

# H<sub>I</sub> intensity mapping with MeerKAT: power spectrum detection in cross-correlation with WiggleZ galaxies

Steven Cunnington<sup>1,2\*</sup>, Yichao Li<sup>3,4†</sup>, Mario G. Santos<sup>4,5</sup>, Jingying Wang<sup>4,6</sup>,  
Isabella P. Carucci<sup>7,8</sup>, Melis O. Irfan<sup>4,9</sup>, Alkistis Pourtsidou<sup>2,10,4</sup>, Marta Spinelli<sup>11,4</sup>,  
Laura Wolz<sup>1</sup>, Paula S. Soares<sup>9</sup>, Chris Blake<sup>12</sup>, Philip Bull<sup>9,4</sup>, Brandon Engelbrecht<sup>4</sup>,  
José Fonseca<sup>13</sup>, Keith Grainge<sup>1</sup>, Yin-Zhe Ma<sup>14,15</sup>

<sup>1</sup>Jodrell Bank Centre for Astrophysics, Department of Physics & Astronomy, The University of Manchester, Manchester M13 9PL, UK

<sup>2</sup>Institute for Astronomy, The University of Edinburgh, Royal Observatory, Edinburgh EH9 3HJ, UK

<sup>3</sup>Department of Physics, College of Sciences, Northeastern University, Wenhua Road, Shenyang, 11089, China

<sup>4</sup>Department of Physics and Astronomy, University of the Western Cape, Robert Sobukwe Road, Cape Town, 7535, South Africa

<sup>5</sup>South African Radio Astronomy Observatory (SARAO), 2 Fir Street, Cape Town, 7925, South Africa

<sup>6</sup>Shanghai Astronomical Observatory, Chinese Academy of Sciences, 80 Nandan Road, Shanghai, 200030, China

<sup>7</sup>Dipartimento di Fisica, Università degli Studi di Torino, via P. Giuria 1, 10125, Torino, Italy

<sup>8</sup>INFN – Istituto Nazionale di Fisica Nucleare, Sezione di Torino, via P. Giuria 1, 10125, Torino, Italy

<sup>9</sup>Department of Physics & Astronomy, Queen Mary University of London, London, E1 4NS, UK

<sup>10</sup>Higgs Centre for Theoretical Physics, School of Physics and Astronomy, The University of Edinburgh, Edinburgh EH9 3FD, UK

<sup>11</sup>Institute of Particle Physics & Astrophysics, Department of Physics, ETH Zurich, Switzerland

<sup>12</sup>Centre for Astrophysics & Supercomputing, Swinburne University of Technology, P.O. Box 218, Hawthorn, VIC 3122, Australia

<sup>13</sup>Instituto de Astrofísica e Ciências do Espaço, Universidade do Porto CAUP, Rua das Estrelas, PT4150-762 Porto, Portugal

<sup>14</sup>NAOC-UKZN Computational Astrophysics Center (NUCAC), University of Kwazulu-Natal, Durban, 4000, South Africa

<sup>15</sup>School of Chemistry and Physics, University of Kwazulu-Natal, Westville Campus, Private Bag X54001, Durban, South Africa

Accepted XXX. Received YYY; in original form ZZZ

## ABSTRACT

We present a detection of correlated clustering between MeerKAT radio intensity maps and galaxies from the WiggleZ Dark Energy Survey. We find a  $7.7\sigma$  detection of the cross-correlation power spectrum, the amplitude of which is proportional to the product of the H<sub>I</sub> density fraction ( $\Omega_{\text{H I}}$ ), H<sub>I</sub> bias ( $b_{\text{H I}}$ ) and the cross-correlation coefficient ( $r$ ). We therefore obtain the constraint  $\Omega_{\text{H I}} b_{\text{H I}} r = [0.86 \pm 0.10 \text{ (stat)} \pm 0.12 \text{ (sys)}] \times 10^{-3}$ , at an effective scale of  $k_{\text{eff}} \sim 0.13 h \text{ Mpc}^{-1}$ . The intensity maps were obtained from a pilot survey with the MeerKAT telescope, a 64-dish pathfinder array to the SKA Observatory (SKAO). The data were collected from 10.5 hours of observations using MeerKAT’s L-band receivers over six nights covering the 11 hr field of WiggleZ, in the frequency range 1015–973 MHz ( $0.400 < z < 0.459$  in redshift). This detection is the first practical demonstration of the multi-dish auto-correlation intensity mapping technique for cosmology. This marks an important milestone in the roadmap for the cosmology science case with the full SKAO.

**Key words:** cosmology: large scale structure of Universe – cosmology: observations – radio lines: general – methods: data analysis – methods: statistical

## 1 INTRODUCTION

Probing the large scale structure of the Universe is a crucial step towards precision cosmology as we try to constrain the nature of dark energy, non-Gaussian fluctuations in the Universe’s primordial density field, and test general relativity. Typically, this is done using galaxy surveys with spectroscopic or photometric redshifts in the optical or near-infrared. At radio wavelengths, we use the redshifted neutral hydrogen (H<sub>I</sub>) hyperfine transition line, with a rest-frame wavelength of 21 cm, to measure redshift. Given the ubiquitous nature

of H<sub>I</sub> in the Universe, we can use it to trace the distribution of dark matter at low and high redshifts.

The faintness of the H<sub>I</sub> emission line makes it challenging to resolve individual galaxies at higher redshifts over large volumes. However, for cosmology we are interested in the bulk fluctuations on large (Mpc) scales, so we can use the H<sub>I</sub> intensity mapping technique. This technique relaxes the requirement of galaxy detection by integrating all 21 cm emission within relatively large spatial voxels (Bharadwaj et al. 2001; Battye et al. 2004; Wyithe et al. 2008; Chang et al. 2008). This delivers high survey speeds over large volumes, providing a novel solution to the current challenges of observational cosmology.

One of the main challenges in detecting the H<sub>I</sub> intensity mapping signal is the presence of foregrounds that are orders of magnitude

\* steven.cunnington@manchester.ac.uk

† liyichao@mail.neu.edu.cn

brighter. Removing these requires precise instrumental calibration. Cross-correlating with galaxy surveys helps to mitigate residual systematics from foregrounds, Radio Frequency Interference (RFI) and thermal noise (Wolz et al. 2016; Pourtsidou et al. 2017). Moreover, it can improve constraints on cosmological parameters and provide insight into the H<sub>I</sub> astrophysics of the correlated galaxies (Anderson et al. 2018; Wolz et al. 2022). Currently, the H<sub>I</sub> intensity mapping signal has only been detected in cross-correlation with galaxy surveys (Masui et al. 2013; Anderson et al. 2018; Li et al. 2021a; Tramonte & Ma 2020; Wolz et al. 2022; CHIME Collaboration et al. 2022).

Both MeerKAT and the future SKA Observatory (SKAO) have been put forward as state-of-the-art intensity mapping instruments capable of complementing and extending cosmological measurements at other wavelengths (SKA Cosmology SWG 2020; Santos et al. 2017). Using the single-dish data from each element of the array (Battye et al. 2013; Bull et al. 2015), we can access the large cosmological scales inaccessible by the interferometer due to its lack of very short baselines. In Wang et al. (2021) we presented the first calibrated maps of a pilot MeerKAT survey, which utilised this single-dish method on the multi-dish interferometer array. In this article, we use this data to measure the cross-correlation power spectrum between the H<sub>I</sub> signal and overlapping WiggleZ data (Drinkwater et al. 2010). With only 10.5 hrs of data for each of the 64 dishes over an effective survey area of  $\sim 200 \text{ deg}^2$ , this detection shows the power of this approach and paves the way towards probing large cosmological scales with much larger surveys on MeerKAT and SKAO.

The paper is structured as follows; in Section 2 we introduce the data products used in this study. Section 3 introduces our approach to foreground cleaning in the MeerKAT intensity maps. The formalism adopted for the power spectrum estimation and modelling is discussed in Section 4. We present our main results in Section 5 and finally conclude in Section 6.

## 2 OBSERVATIONAL DATA

The MeerKAT H<sub>I</sub> intensity mapping data was collected using the L-band with 10.5 hours of observation per dish over six nights between February and July 2019. The L-band has 4096 frequency channels at 856 – 1712 MHz, but in this work, we only use 199 channels at 973.2 – 1014.6 MHz ( $0.400 < z < 0.459$ ). Of these channels, a further 32 are removed due to their dominant contributions to the eigenmodes of the principal component analysis (see later discussion in Section 3) for those particular channels. This aggressive strategy can be seen as a final RFI-flagging stage<sup>1</sup> and was necessary in order for us to obtain a cross-correlation detection. The survey area spans around  $200 \text{ deg}^2$  and targeted the WiggleZ 11 hr field, covering  $153^\circ < \text{R.A.} < 172^\circ$  and  $-1^\circ < \text{Dec.} < 8^\circ$  (Drinkwater et al. 2010; Blake et al. 2010; Drinkwater et al. 2018). In this analysis, only the auto-correlation of MeerKAT interferometer visibility data, i.e. the single dish mode observation, is used. The time-ordered data for each dish,  $d$ , are projected into the map space via the map-making process (Tegmark 1997),

$$\hat{m} = (A^T N^{-1} A)^{-1} A^T N^{-1} d \quad (1)$$

in which  $A$  is the pointing matrix mapping the time-ordered data to the map coordinates and  $N$  is the noise covariance matrix between time stamps. As described in Wang et al. (2021), the time-ordered data (TOD) is calibrated against a noise diode which is fired every

20 seconds. This removes long-term noise correlation, so-called 1/f noise, due to receiver chain gain variations on time scales longer than 20 s. On shorter time scales, 1/f noise is negligible compared to thermal noise fluctuations (Li et al. 2021b). We also subtract the average signal every 220 s in the TOD which suppresses long-term sloping gain changes. This should reduce the overall variance of the signal but can potentially have the adverse effect of removing H<sub>I</sub> signal over large angular scales. In this work we assume any signal loss from this process is sub-dominant relative to the signal loss from foreground cleaning and thus do not attempt any reconstruction.

The noise covariance matrix  $N$  is assumed to be diagonal with constant variance during the observation, but we allow the variance to differ between dishes. The noise covariance is also projected to the map space via,

$$\hat{n} = (A^T N^{-1} A)^{-1}, \quad (2)$$

where  $\hat{n}$  is the pixel noise variance. The inverse of the pixel noise variance,  $w_{\text{H}_I} = 1/\hat{n}$ , is used as the inverse-variance weight in the analysis<sup>2</sup>. We use the flat-sky approximation and grid the map into square pixels with a width of  $0.25^\circ$ . To create the final maps, we average over all individual dish maps (full details of the single-dish calibration are provided in Wang et al. (2021)).

The observed intensity maps are shown in Figure 1. The top panel shows the frequency-averaged intensity map before foreground cleaning. The bottom panel shows the residual map after foreground cleaning, a process we outline in the following section.

## 3 FOREGROUND CLEANING

Here we discuss the foreground cleaning performed on the MeerKAT intensity maps. We provide detailed descriptions on each stage in the following sub-sections but begin with a summary of the foreground cleaning method we adopt.

The foreground cleaning is performed using a blind Principal Component Analysis (PCA) method, which relies on the foregrounds being the dominant signal and correlated in frequency. Thus, by removing the first  $N_{\text{fg}}$  principal component modes in frequency from each pixel, the majority of their contribution is suppressed (see Section 3.2 for further discussion). Before cleaning, the map is resmoothed using a Gaussian window function with kernel size 1.2 times the largest beam size within the frequency range (see Section 3.1 for details). Foreground cleaning is imperfect, and the cleaned maps contain residual foreground structure which can be seen by comparing both panels in Figure 1. However, the amplitude of the map has decreased by several orders of magnitude, thus the foreground residuals should dominate less over the H<sub>I</sub> fluctuations. Furthermore, some H<sub>I</sub> signal will be removed, typically on larger scales where modes are most degenerate with the spectrally smooth foregrounds. We aim to reconstruct this lost signal with a foreground transfer function, which we discuss in Section 3.3.

### 3.1 Deconvolution of maps

It is understood that a frequency-dependent beam size can cause the foregrounds to leak into a greater number of spectral modes, requiring more aggressive cleaning (Switzer et al. 2015; Alonso et al. 2015).

<sup>2</sup> We adopt the H<sub>I</sub> in the subscript of  $w_{\text{H}_I}$  to maintain a consistent notation with later formalism where they require distinguishing from the galaxy weights.

<sup>1</sup> Full details of the initial RFI-flagging are given in Wang et al. (2021).

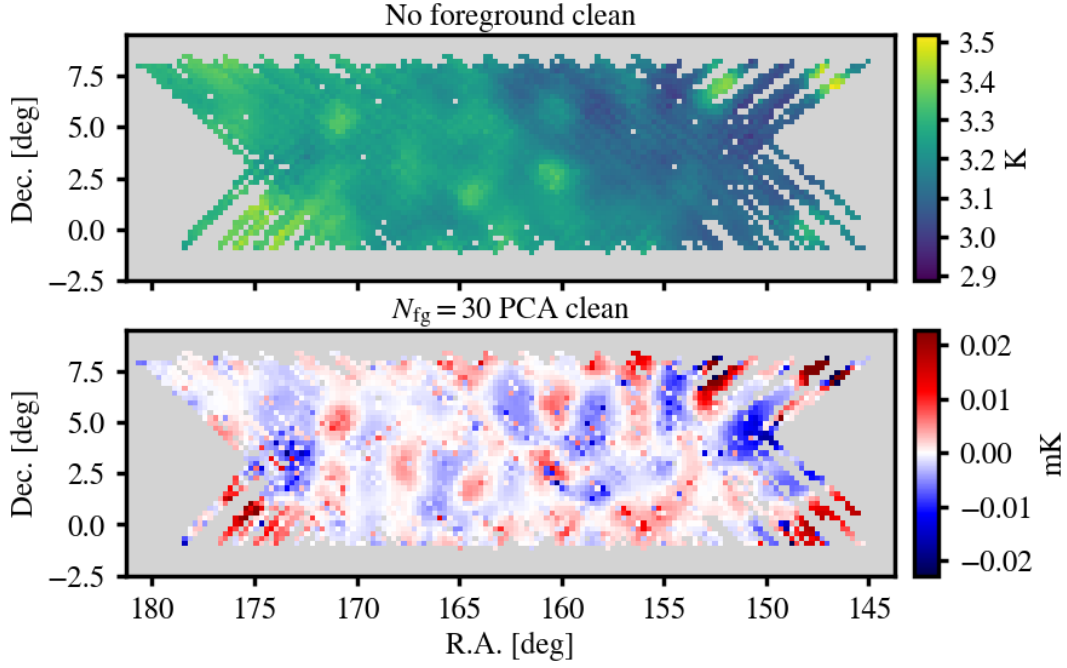


**Figure 1.** Calibrated MeerKAT intensity maps in the WiggleZ 11hr field averaged over the 199 frequency channels covering  $1014.6 > \nu > 973.2$  MHz ( $0.400 < z < 0.459$ ). Top panel is before foreground cleaning and bottom panel is after  $N_{\text{fg}} = 30$  PCA modes have been subtracted (foreground clean performed before averaging through frequency).

A way to potentially mitigate this issue is to convolve all maps to a common resolution before performing the foreground clean, as done in previous experiments (Masui et al. 2013; Wolz et al. 2017; Anderson et al. 2018; Wolz et al. 2022). However, recent tests on simulations suggest that a simple Gaussian resmoothing of the data to a common resolution does not improve blind foreground removal techniques, even if the true beam is a perfect Gaussian (Matshawule et al. 2021; Spinelli et al. 2021). For real data though, it is beneficial to resmooth to homogenise some of the systematic contributions from e.g. residual RFI or polarisation leakage. For this reason we perform a weighted resmoothing on the MeerKAT H<sub>i</sub> intensity maps prior to foreground cleaning.

An intensity map  $\delta T'$  which has a frequency dependent beam (denoted by the ' index) with a full-width-half-maximum  $\theta_{\text{FWHM}}(\nu)$  in degrees, and an angular separation between pixels given by  $\Delta\theta$ , is convolved with the following kernel:

$$K(\Delta\theta, \nu) = \exp \left[ -\frac{\Delta\theta^2}{2[\gamma\sigma_{\text{max}}^2 - \sigma^2(\nu)]} \right], \quad (3)$$

where  $\sigma(\nu) = \theta_{\text{FWHM}}(\nu)/(2\sqrt{2\ln 2})$ ,  $\sigma_{\text{max}}$  is the maximum  $\sigma(\nu)$  value and  $\gamma$  is a scaling factor which governs how much the final effective resolution is decreased by.

In previous Green Bank Telescope (GBT) studies, a choice of  $\gamma = 1.4$  was used (Masui et al. 2013). In this work, due to the already large MeerKAT beam, we use a smaller value of  $\gamma = 1.2$ . We experimented with this choice, finding  $\gamma = 1$  produced a noisier power spectrum with worse model agreement. The higher choice of  $\gamma = 1.4$  delivered a similarly good model agreement compared to  $\gamma = 1.2$ , but had a slightly lower cross-correlation detection significance due to the increased damping at high- $k$ . Not performing any reconvolution still delivered a clear detection but resulted in a particularly noisy power spectrum at small- $k$ , indicating the presence of residual

foreground and systematics which are mitigated by this resmoothing procedure.

The kernel in Equation 3 is normalised such that the sum over all pixels is equal to unity, then the weighted convolution used to resmooth the maps is given by

$$\delta T(\theta, \nu) = \frac{[\delta T'(\theta, \nu) w'_{\text{Hi}}(\theta, \nu)] * K(\Delta\theta, \nu)}{w'_{\text{Hi}}(\theta, \nu) * K(\Delta\theta, \nu)}, \quad (4)$$

where  $w'_{\text{Hi}}(\theta)$  is the inverse variance weight. The  $*$  denotes a convolution performed separately in each frequency channel e.g.  $w'_{\text{Hi}}(\theta) * K(\Delta\theta) = \sum_i w'_{\text{Hi}}(\theta_i) K(\theta - \theta_i)$ . To ensure the weight field still represents the inverse variance of the new resmoothed field, the weight  $w'_{\text{Hi}}$  is convolved according to

$$w_{\text{Hi}}(\theta, \nu) = \frac{[w'_{\text{Hi}}(\theta, \nu) * K(\Delta\theta, \nu)]^2}{w'_{\text{Hi}}(\theta, \nu) * K^2(\Delta\theta, \nu)}. \quad (5)$$

### 3.2 PCA foreground cleaning

In this work, a PCA-based blind foreground subtraction method is used. The observed intensity maps can be represented by a matrix  $\mathbf{X}_{\text{obs}}$  with dimensions  $N_\nu \times N_\theta$  where  $N_\nu$  is the number of frequency channels along the line-of sight and  $N_\theta$  is the number of pixels. The assumption behind blind-foreground cleaning is that the data can be represented by the linear system  $\mathbf{X}_{\text{obs}} = \hat{\mathbf{A}}\mathbf{S} + \mathbf{R}$ , where  $\hat{\mathbf{A}}$  represents the mixing matrix and  $\mathbf{S}$  are the  $N_{\text{fg}}$  separable source maps identified by projecting the mixing matrix along the data  $\mathbf{S} = \hat{\mathbf{A}}^T \mathbf{X}_{\text{obs}}$ . In PCA, the mixing matrix is extracted from the eigen-decomposition of the frequency covariance matrix of the mean-centred data, defined by  $\mathbf{C} = (\mathbf{w}\mathbf{X}_{\text{obs}})^T (\mathbf{w}\mathbf{X}_{\text{obs}}) / (N_\theta - 1)$ , where  $\mathbf{w}$  are the inverse variance weights recast into  $N_\nu \times N_\theta$  matrices. The eigen-decomposition is then given as  $\mathbf{C}\mathbf{V} = \mathbf{V}\mathbf{\Lambda}$ , where  $\mathbf{\Lambda}$  is the diagonal matrix of eigenvalues ordered by descending magnitude, and  $\mathbf{V}$  are the eigenvectors, the

first  $N_{\text{fg}}$  of which supplies the set of functions used to construct the mixing matrix. We assume the subtraction of  $\hat{\mathbf{A}}\mathbf{S}$  in the linear system will remove dominant foregrounds, leaving behind in the residuals  $\mathbf{R}$  any H<sub>I</sub> signal not removed in the subtraction.

### 3.3 Transfer function construction

We compensate the signal loss due to the foreground cleaning with a foreground transfer function. Following previous literature (Masui et al. 2013; Switzer et al. 2013, 2015), the transfer function can be constructed by injecting mock intensity mapping data  $\mathbf{M}_{\text{H}_I}$  into the true observed data  $\mathbf{X}_{\text{obs}}$ , which includes foregrounds and observational systematics. By running a PCA clean on this combination, we can measure (and compensate for) the signal loss in the cleaned mock data;

$$\mathbf{M}_{\text{c}} = [\mathbf{M}_{\text{H}_I} + \mathbf{X}_{\text{obs}}]_{\text{PCA}} - [\mathbf{X}_{\text{obs}}]_{\text{PCA}}. \quad (6)$$

The  $[\ ]_{\text{PCA}}$  notation represents performing the PCA clean (outlined in Section 3.2) on the quantities inside the brackets, treating them as a single combination. For example, the mixing matrix is not determined separately for both mock and data in  $[\mathbf{M}_{\text{H}_I} + \mathbf{X}_{\text{obs}}]_{\text{PCA}}$ , but determined for the combination of  $\mathbf{M}_{\text{H}_I} + \mathbf{X}_{\text{obs}}$ . We also subtract the PCA clean of the data,  $[\mathbf{X}_{\text{obs}}]_{\text{PCA}}$ , since this only adds uncorrelated variance, thus subtracting it makes convergence to a smooth transfer function more efficient, requiring fewer mock iterations. After calculating  $\mathbf{M}_{\text{c}}$ , we measure the cross-power spectrum with a corresponding mock galaxy map  $\mathbf{M}_{\text{g}}$ , then divide this by a foreground-free equivalent to estimate the signal loss at each mode;

$$\mathcal{T}(k) = \left\langle \frac{\mathcal{P}(\mathbf{M}_{\text{c}}, \mathbf{M}_{\text{g}})}{\mathcal{P}(\mathbf{M}_{\text{H}_I}, \mathbf{M}_{\text{g}})} \right\rangle. \quad (7)$$

$\mathcal{P}()$  denotes an operator which measures the cross-power spectrum, then spherically averages modes into the same  $k$ -bins as the data. The angled brackets represent an ensemble average over a large number of mocks (we use 100 in this work).

The H<sub>I</sub> mocks are generated with the lognormal method (Coles & Jones 1991), sampled from a model H<sub>I</sub> power spectrum (the same as that used in the power spectrum fitting, see Section 4.1) with a Gaussian smoothing applied perpendicular to the line-of-sight to approximately emulate the MeerKAT beam. Similarly, for the galaxy mocks, we generate a lognormal density field with the same random seed as the H<sub>I</sub>, then Poisson sample galaxies onto the field with the same number count as the WiggleZ catalogue. These steps ensure the mock fields emulate the amplitudes of real maps as realistically as possible. There is evidence suggesting the transfer function is not overly sensitive to the choice of fiducial cosmology (Cunnington 2022), but further investigation into how much it can be relied on for precision cosmology is required.

Any power spectrum measurement we make on the data is divided by  $\mathcal{T}(k)$  to correct for the signal loss (unless clearly stated in demonstrative figures). For the H<sub>I</sub> auto-power spectrum used in the error estimation (discussed later in Section 4), we also multiply through by  $1/\mathcal{T}(k)$ . Previous studies have opted to use  $1/\mathcal{T}(k)^2$  as a correction instead (Switzer et al. 2013), motivated by the assumption that in auto-correlation, signal loss occurs in both maps, so there should be twice the reconstruction of power needed. However, from simulation tests, we found this over-corrected the signal loss. Furthermore, our analytical error estimation on the cross-power spectrum (see Section 4), which uses the auto-H<sub>I</sub> power spectrum, is found to be in good agreement with other approaches of error estimation using the WiggleZ randoms and jackknife tests.  $\chi^2_{\text{dof}}$  analysis also suggests our errors are not over-estimated in any case. This changes if we opt for

the  $1/\mathcal{T}(k)^2$  correction where it becomes clear that the errors have been over-estimated, suggesting that the signal loss in the auto-H<sub>I</sub> power spectrum has been over-corrected. We defer further investigation into signal loss in the H<sub>I</sub> auto-correlation to future work.

## 4 POWER SPECTRUM ESTIMATION & MODELLING

The power spectrum estimation process we adopt is based on the optimal weighting method outlined in Feldman et al. (1994) (see Wolz et al. (2017); Blake (2019) for applications to H<sub>I</sub> intensity mapping cross-correlations). We define the two Fourier transformed fields of the H<sub>I</sub> temperature fluctuation maps  $\delta T_{\text{H}_I}$  and the galaxy count field  $n_{\text{g}}$  as

$$\tilde{F}_{\text{H}_I}(\mathbf{k}) = \sum_{\mathbf{x}} \delta T_{\text{H}_I}(\mathbf{x}) w_{\text{H}_I}(\mathbf{x}) \exp(i\mathbf{k} \cdot \mathbf{x}) \quad (8)$$

$$\tilde{F}_{\text{g}}(\mathbf{k}) = \sum_{\mathbf{x}} n_{\text{g}}(\mathbf{x}) w_{\text{g}}(\mathbf{x}) \exp(i\mathbf{k} \cdot \mathbf{x}) - N_{\text{g}} \tilde{W}_{\text{g}}(\mathbf{k}), \quad (9)$$

where  $N_{\text{g}} = \sum n_{\text{g}}$  is the total number of galaxies in the optical map and  $\tilde{W}_{\text{g}}$  is the weighted Fourier transform of the selection function ( $W_{\text{g}}$ ) which is normalised such that  $\sum_{\mathbf{x}} W_{\text{g}}(\mathbf{x}) = 1$ ;

$$\tilde{W}_{\text{g}}(\mathbf{k}) = \sum_{\mathbf{x}} W_{\text{g}}(\mathbf{x}) w_{\text{g}}(\mathbf{x}) \exp(i\mathbf{k} \cdot \mathbf{x}). \quad (10)$$

The selection function  $W_{\text{g}}$  accounts for incompleteness in the WiggleZ survey and is constructed by stacking the random catalogues generated in Blake et al. (2010), reproducing the varying target and redshift completeness. The map weights in the above equations are the inverse variance map for the H<sub>I</sub> field<sup>3</sup>,  $w_{\text{H}_I}(\mathbf{x}) = 1/\hat{n}(\mathbf{x})$  (defined in Section 2) and for the galaxies we use the optimal weighting as per Feldman et al. (1994)

$$w_{\text{g}}(\mathbf{x}) = 1 / \left( 1 + \frac{W_{\text{g}}(\mathbf{x}) N_{\text{g}} P_0}{V_{\text{cell}}} \right), \quad (11)$$

where  $P_0$  is a chosen value of the power spectrum at the scale where an optimal measurement is sought. We use  $P_0 = 5000 h^{-3} \text{Mpc}^3$ , approximately corresponding to  $k = 0.1 h \text{Mpc}^{-1}$ .  $V_{\text{cell}}$  is the volume of a grid cell in  $h^{-3} \text{Mpc}^3$ . The maps are enclosed onto a cuboid in comoving space, using a fiducial Planck18 (Planck Collaboration et al. 2020) cosmology with sides of length  $(l_x, l_y, l_z) \sim (812, 264, 176) \text{Mpc}/h$ , divided into  $(n_x, n_y, n_z) = (151, 49, 250)$  equal sized cells. Assuming a flat-sky approximation, and using the map pixel's angular coordinates and redshifts, we grid the data using a nearest grid point assignment<sup>4</sup>. To taper the edges along the line-of-sight, we apply a Blackman window along the  $z$ -axis of the galaxy and H<sub>I</sub> intensity maps, as well as their weights and selection functions. The cross-correlation between the H<sub>I</sub> intensity maps and the galaxies is then estimated with

$$\hat{P}_{\text{H}_I, \text{g}}(\mathbf{k}) = \frac{V_{\text{cell}}}{\sum_{\mathbf{x}} w_{\text{H}_I}(\mathbf{x}) w_{\text{g}}(\mathbf{x}) W_{\text{g}}(\mathbf{x})} \text{Re} \left\{ \tilde{F}_{\text{H}_I}(\mathbf{k}) \cdot \tilde{F}_{\text{g}}^*(\mathbf{k}) \right\} \frac{1}{N_{\text{g}}}. \quad (12)$$

Similarly, the H<sub>I</sub> and galaxy auto-power spectra, which are needed for the error estimation (see below), are given by

$$\hat{P}_{\text{H}_I}(\mathbf{k}) = \frac{V_{\text{cell}}}{\sum_{\mathbf{x}} w_{\text{H}_I}^2(\mathbf{x})} |\tilde{F}_{\text{H}_I}(\mathbf{k})|^2, \quad (13)$$

<sup>3</sup> Optimal weights for H<sub>I</sub> intensity mapping are derived in Blake (2019) and we leave it to future work on data with higher  $S/N$  to experiment with these.

<sup>4</sup> The scales that we probe and the  $S/N$  of this data means potential impact from aliasing effects (Jing 2005) are sub-dominant and we do not need to correct for them.



$$\hat{P}_g(k) = \frac{V_{\text{cell}}}{\sum_{\mathbf{x}} w_g^2(\mathbf{x}) W_g^2(\mathbf{x})} \left[ |\tilde{F}_g(\mathbf{k})|^2 - S_g \right] \frac{1}{N_g^2}, \quad (14)$$

where  $S_g$  accounts for the shot noise in the galaxy survey, given as

$$S_g = N_g \sum_{\mathbf{x}} w_g^2(\mathbf{x}) W_g^2(\mathbf{x}). \quad (15)$$

These power spectra are all spherically averaged into bandpowers  $|\mathbf{k}| \equiv k$  to provide the final 1D power spectra results (the cross- and H<sub>I</sub>-auto power spectra are also corrected with the  $1/\mathcal{T}(k)$  as discussed in Section 3.3). For noise-dominated H<sub>I</sub> intensity maps, the errors for the cross-power can be estimated analytically from

$$\hat{\sigma}_{\text{H}_I, g}(k) = \frac{1}{\sqrt{2N_m(k)}} \sqrt{\hat{P}_{\text{H}_I, g}^2(k) + \hat{P}_{\text{H}_I}(k) \left( \hat{P}_g(k) + \frac{1}{\bar{n}_g} \right)}, \quad (16)$$

where  $N_m$  is the number of modes in each  $k$ -bin and  $\bar{n}_g = N_g/(l_x \times l_y \times l_z)$  is the number density of galaxies. The  $1/\sqrt{2}$  factor in Equation 16 appears because this is the error on a cross-correlation of two fields, so the number of independent pairs available to measure the variance on the mean doubles. We compared these analytical error estimations to ones calculated from cross-correlating the MeerKAT data with the random WiggleZ catalogues used to derive the selection function, finding very good agreement across all scales. Furthermore, we also found good agreement with an internal error estimation which used a jackknife approach (Norberg et al. 2009).

#### 4.1 Theoretical modelling

We fit a model to the cross-power spectrum which is given by

$$P_{\text{H}_I, g}(\mathbf{k}) = \bar{T}_{\text{H}_I} b_{\text{H}_I} b_g r (1 + f\mu^2)^2 P_m(k) \times \exp \left[ \frac{-(1 - \mu^2)k^2 R_{\text{beam}}^2}{2} \right], \quad (17)$$

where  $\bar{T}_{\text{H}_I}$  is the mean H<sub>I</sub> temperature of the field in mK,  $b_{\text{H}_I}$  and  $b_g$  are the H<sub>I</sub> and galaxy biases and  $r$  is the cross-correlation coefficient. We account for linear redshift-space distortions (RSD) with the  $(1 + f\mu^2)^2$  factor (Kaiser 1987), where  $f$  is the growth rate of structure and  $\mu$  is the cosine of the angle from the line-of-sight.  $P_m$  is the matter power spectrum produced using CAMB (Lewis et al. 2000) with a Planck18 (Planck Collaboration et al. 2020) cosmology. The exponential factor approximates the smoothing of perpendicular modes due to the MeerKAT beam, where  $R_{\text{beam}}$  is the standard deviation of the Gaussian beam profile in comoving units, taking into account the reconvolution as explained in Section 3.1, which gives  $R_{\text{beam}} = 13.3 \text{ Mpc } h^{-1}$ .

To fully account for RSD, the model in Equation 17 should be (not including the beam damping for brevity)

$$P_{\text{H}_I, g}(\mathbf{k}) = \bar{T}_{\text{H}_I} \left[ r b_{\text{H}_I} b_g + b_{\text{H}_I} f\mu^2 + b_g f\mu^2 + f^2\mu^4 \right] P_m(k), \quad (18)$$

which accounts for the biases appearing in cross-terms from the expansion of the two fields in redshift space  $\delta_{\text{H}_I}^s(\mathbf{k}) = b_{\text{H}_I} \delta_m(\mathbf{k}) + f\mu \theta(\mathbf{k})$  and  $\delta_g^s(\mathbf{k}) = b_g \delta_m(\mathbf{k}) + f\mu \theta(\mathbf{k})$ , where  $\theta(\mathbf{k})$  is the velocity divergence field<sup>5</sup>. However, we are only attempting a fit to the spherically-averaged power spectrum

monopole, which is uniformly averaged across  $\mu$ . This would make  $b_{\text{H}_I}$  perfectly degenerate with  $\bar{T}_{\text{H}_I} r$ . To break this degeneracy we would need to introduce an anisotropic sensitivity on  $\mu$  in our analysis, achieved by modelling the quadrupole (Cunnington et al. 2020; Soares et al. 2021). This would require a higher  $S/N$  than we have available from the MeerKAT pilot survey data. This is why we follow previous literature (Wolz et al. 2022) and probe the degenerate quantity  $\bar{T}_{\text{H}_I} b_{\text{H}_I} r$ , but include a matter-only RSD, to avoid biasing the amplitude of the power spectrum by the  $(1 + f\mu^2) \sim 1.7$  Kaiser term.

The model in Equation 17 is discretised onto the same 3D grid of modes as the data and then convolved with the survey window functions

$$P_{\text{H}_I, g}(\mathbf{k}) \rightarrow P_{\text{H}_I, g} * W_{\text{H}_I} W_g = \frac{\sum_i P_{\text{H}_I, g}(\mathbf{k}_i') \text{Re} \{ \tilde{W}_g(\mathbf{k} - \mathbf{k}_i') \tilde{W}_{\text{H}_I}(\mathbf{k} - \mathbf{k}_i')^* \}}{\sum w_g(\mathbf{x}) w_{\text{H}_I}(\mathbf{x}) W_g(\mathbf{x}) W_{\text{H}_I}(\mathbf{x})}. \quad (19)$$

In lieu of a precisely constructed survey selection function  $W_{\text{H}_I}$  for the H<sub>I</sub> intensity maps, we use a simple binary window function that is 1 wherever a pixel is filled and 0 otherwise. The convolved model in Equation 19 is spherically averaged into the same  $k$ -bins as the data.

The mean H<sub>I</sub> temperature  $\bar{T}_{\text{H}_I}$  can be recast to the H<sub>I</sub> density fraction ( $\Omega_{\text{H}_I}$ ) using (Battye et al. 2013)

$$\bar{T}_{\text{H}_I}(z) = 180 \Omega_{\text{H}_I}(z) h \frac{(1+z)^2}{\sqrt{\Omega_m(1+z)^3 + \Omega_\Lambda}} \text{ mK}, \quad (20)$$

where  $\Omega_m$  and  $\Omega_\Lambda$  are the density fractions for matter and the cosmological constant, respectively. Thus fitting the amplitude of the cross-power spectrum allows us to constrain  $\Omega_{\text{H}_I} b_{\text{H}_I} r$ . When fitting  $\Omega_{\text{H}_I} b_{\text{H}_I} r$  to the power spectrum data using the model in Equation 17, we fix the galaxy bias ( $b_g$ ) and growth rate ( $f$ ), since they are well constrained from other experiments relative to the other parameters. We assume  $f = 0.737$  (based on  $f \sim \Omega_m(z)^\gamma$ , where  $\gamma = 0.545$  (Linder 2005; Planck Collaboration et al. 2020)) and  $b_g = 0.911$  (Blake et al. 2011) at the central redshift of our data ( $z_{\text{eff}} = 0.43$ ).

## 5 RESULTS

### 5.1 H<sub>I</sub> auto power spectrum

The auto power spectrum of the cleaned H<sub>I</sub> intensity maps gives some indication of how much foregrounds have been suppressed. In Figure 2 we show the 2D auto-H<sub>I</sub> power spectrum decomposed into anisotropic  $k$ -bins perpendicular ( $k_\perp = \sqrt{k_x^2 + k_y^2}$ ) and parallel ( $k_\parallel \equiv k_z$ ) to the line-of-sight. The far-left panel shows the original data before foreground removal, demonstrating the dominance of the foregrounds and their concentration on the largest scales, particularly at small- $k_\parallel$ . Removing just a few principal components reduces the amplitude of the auto power spectrum by several orders of magnitude, as shown in the second panel. In simulation tests, removing  $N_{\text{fg}} \sim 4$  PCA modes is sufficient to remove the majority of the foregrounds (Alonso et al. 2015; Cunnington et al. 2021), and this should also be the case for a perfectly designed and calibrated experiment. The resulting cleaned maps in this idealised case would contain H<sub>I</sub> signal and Gaussian thermal noise, similar to the model in the fifth panel of Figure 2. The thermal noise in the ideal model is large due to the survey's low observing time. This yields an auto power spectrum am-

<sup>5</sup> The cross-correlation coefficient  $r$  only enters on cross-correlation between biased density terms.

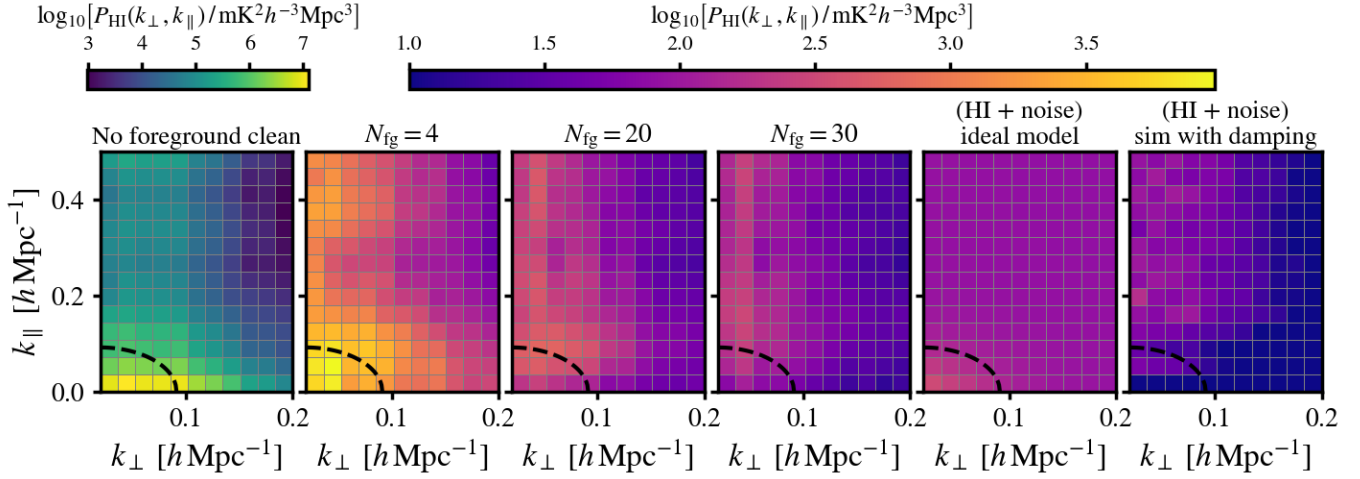


**Figure 2.** MeerKAT HI auto power spectra at  $0.400 < z < 0.459$  decomposed into  $k_{\perp}$  and  $k_{\parallel}$  modes for different foreground cleans indicated by  $N_{\text{fg}}$  (the number of PCA modes removed). The fifth panel shows a predicted level for the HI signal plus purely Gaussian thermal noise, in an ideal case assuming no signal loss. The thermal noise is predicted to be  $\sim 2$  mK for this survey (estimated in Wang et al. (2021)). The far-right panel shows a simulation of HI plus Gaussian noise including signal damping from the beam, additional resmoothing and foreground cleaning. The black-dashed line marks a characteristic scale of  $|k| = 0.08 h \text{ Mpc}^{-1}$  (approximately the scale of the first BAO wiggle maximum) at which, from our modelling, we would expect the HI power to be  $P_{\text{HI}} \sim 100 \text{ mK}^2 h^{-3} \text{ Mpc}^3$ , i.e.  $\log_{10}[P_{\text{HI}}] = 2$ . None of these power spectra have had signal loss reconstructed by the transfer function.

plitude of  $P_{\text{noise}} \sim 85 \text{ mK}^2 h^{-3} \text{ Mpc}^3$ , which is expected to dominate over the HI signal<sup>6</sup> on most scales, as seen in the Figure 2 model.

For this pilot-survey data, there will be instrumental calibration imperfections, residual RFI and other systematics (see discussions in Irfan et al. (2021)). The instrumental response modulates the foregrounds, resulting in additional spectral structure that requires more PCA modes to be removed. Uncleaned modes containing residual foregrounds, RFI and other systematics will positively bias the auto-power spectrum<sup>7</sup>. This is why for the  $N_{\text{fg}} = 4$  case, we do not reach the level of the HI signal plus noise.

As  $N_{\text{fg}}$  increases in Figure 2, the amplitude of the power drops, and this occurs more severely for large modes, particularly at small- $k_{\parallel}$ . While it appears that we are reaching below the idealised HI + noise model at high- $k_{\perp}$  and low- $k_{\parallel}$  in the  $N_{\text{fg}} \geq 20$  cases, we would need to account for the effects of the map deconvolution and the foreground clean, both of which would damp the HI + noise model further. In the far-right panel we show a simulated HI mock with the same noise level as the idealised model, but include some observational effects. To emulate the beam and reconvolution, we smooth the simulation perpendicular to the line-of-sight. We also emulate signal loss from the foreground clean by projecting out modes based on the same PCA mixing matrix functions derived for the  $N_{\text{fg}} = 30$  data case. Comparison between the  $N_{\text{fg}} = 30$  and far-right panel suggests we have not reached the estimated auto-power spectrum level, indicating that residual RFI, foregrounds, and other systematics are present in the data.

Since the additive bias from non-cosmological residuals is unknown, it is difficult to compare auto-correlated data and model and conclude that a cosmological detection has been achieved. Cross-correlating with galaxy surveys avoids these additive biases, serving

the motivation for this work. We leave a detailed study into the auto-HI power for future work, where we will explore cross-correlating different sets of dishes or observational time-blocks (a method adopted in GBT experiments (Masui et al. 2013)).

## 5.2 Post-foreground clean signal reconstruction

Along with residuals from an imperfect cleaning process, foreground removal will also cause cosmological signal loss in the intensity maps, which requires reconstruction to avoid negatively biasing the measured power spectrum. To do this, we follow previous literature (Masui et al. 2013; Anderson et al. 2018; Wolz et al. 2022) and implement a foreground transfer function (Switzer et al. 2015). The transfer function is constructed by injecting simulated mock maps with a known signal into the real data, as discussed in Section 3.3.

We plot the Fourier-space transfer function  $\mathcal{T}(k_{\perp}, k_{\parallel})$  in Figure 3 (3 left panels) as well as  $\mathcal{T}(k)$  (far-right panel). As seen in the auto-HI power spectrum in Figure 2, after foreground cleaning there is still evidence of residual systematics, which rival the amplitude of the HI signal. However, as the  $\mathcal{T} < 1$  values in Figure 3 show, the foreground cleaning is causing signal loss, mostly in the small- $k_{\parallel}$  modes. Thus, a fine balance is required between reducing foreground residuals and limiting cosmological signal loss.

Encouragingly, we found we were still able to obtain a  $> 4\sigma$  cross-correlation detection with the overlapping WiggleZ galaxies even when the transfer function is not used to correct for signal loss, as we will demonstrate in the following section. However, using the transfer function avoids biasing parameter estimates and improves the cross-correlation detection. We therefore still implement it in the cross-correlation results, which we present next.

## 5.3 Cross-correlation with WiggleZ galaxies

There are 4031 galaxies in the overlapping 11 hr field of the WiggleZ galaxy survey (Drinkwater et al. 2010, 2018). Following the steps outlined in Section 4, we compute an estimate for the cross-power

<sup>6</sup> We assume  $\Omega_{\text{H}} b_{\text{H}} = 0.85 \times 10^{-3}$  for the HI model and simulation in Figure 2.

<sup>7</sup> This assumes these systematics have not caused the gain to be systematically overestimated.

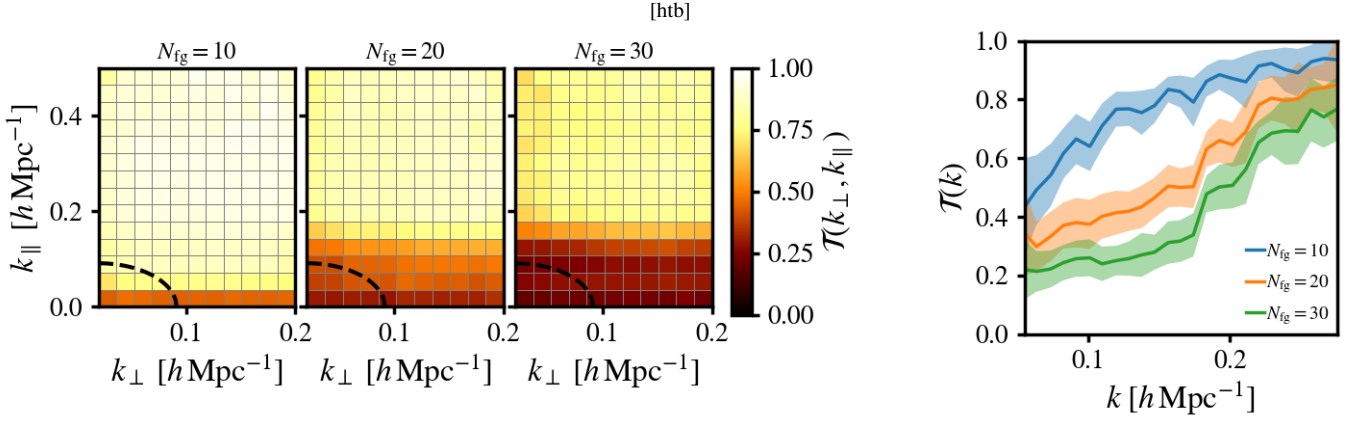


**Figure 3.** Foreground transfer functions used to correct for the signal loss in the power spectrum measurement from foreground cleaning. Details of its construction are given in Section 3.3. A value of  $\mathcal{T}=1$  denotes no signal loss, while  $\mathcal{T} \ll 1$  denotes severe signal loss. Three-left panels show the transfer function decomposed into  $k_{\perp}$  and  $k_{\parallel}$  modes for different foreground cleans indicated by  $N_{\text{fg}}$ . As in Figure 2, the black-dashed line marks a characteristic scale of  $|k| = 0.08 \, h \, \text{Mpc}^{-1}$  (approximately the scale of the first BAO wiggle maximum). Far-right panel shows the transfer function binned into the same spherically averaged  $k$ -bins as those used for the main power spectrum estimation. The shaded regions indicate the  $1\sigma$  errors estimated from the variance in the 100 simulations used in the construction of  $\mathcal{T}(k)$ .

spectrum between the WiggleZ galaxies and the MeerKAT intensity maps, foreground cleaned by removing  $N_{\text{fg}} = 30$  PCA modes. We present this power spectrum in Figure 4. The middle panel shows the signal-to-noise ratio, where we find  $S/N \sim 2$  on large scales. We use an analytical method to estimate the errors (discussed in Section 4). At smaller scales, the MeerKAT beam (Asad et al. 2021; de Villiers & Cotton 2022), which is significantly larger than previous intensity mapping surveys<sup>8</sup> (Masui et al. 2013; Anderson et al. 2018), is the main reason for the poor  $S/N$ .

The model (black-dotted line) in Figure 4 is calculated following Section 4.1. In this model, we fix all parameters to fiducial quantities except for the degenerate quantity  $\bar{T}_{\text{H I}} b_{\text{H I}} r$  for which we assume scale-independence, hence this quantity will only affect the amplitude of the model. Thus, by fitting the amplitude of the cross-power spectrum, we are sensitive to  $\Omega_{\text{H I}} b_{\text{H I}} r$  (from the relation in Equation 20). We quote the best-fit value for  $\Omega_{\text{H I}} b_{\text{H I}} r$  in the top-right of Figure 4, which was fitted to the data using a least-squares method. We discuss the parameter constraints on  $\Omega_{\text{H I}}$  in the following section.

We find a good agreement ( $\chi^2_{\text{dof}} \sim 1$ )<sup>9</sup> between the data and model across all scales ( $0.05 < k < 0.28 \, h \, \text{Mpc}^{-1}$ ) in Figure 4. Furthermore, we analyse  $\sqrt{\Delta\chi^2} \equiv \sqrt{\chi^2 - \chi^2_{\text{null}}}$ , the difference between the data's  $\chi^2$  evaluated using our cross-correlation model, and one using a null model with zero cross-power. This quantifies the statistical significance of the cross-correlation detection. We achieve a  $7.7\sigma$  detection, providing strong evidence for the first verification of a cosmological signal with a multi-dish array performing single-dish intensity mapping.

We conducted various null tests on the analysis pipeline. The bottom panel of Figure 4 shows the results from shuffling the galaxy maps along the line-of-sight, which should destroy the cross-correlation clustering signal. We re-ran the power spectrum estimation

pipeline after each shuffle and found a result consistent with zero. We found similar null results when shuffling the cleaned H I intensity maps along the line-of-sight and swapping the WiggleZ maps with random mocks from Blake et al. (2010).

We did not apply the transfer function in the bottom panel of Figure 4, since scaling the null results would make no difference. We were still able to obtain a detection for the original un-shuffled results where a transfer function has also not been used. This provides a  $> 4\sigma$  detection, which is strong evidence for correlated clustering since this result relied on no signal reconstruction.

For the power spectrum in Figure 4 we chose  $N_{\text{fg}} = 30$  as it offers the best balance between goodness-of-fit ( $\chi^2_{\text{dof}}$ ) and detection significance ( $\sqrt{\Delta\chi^2}$ ). Figure 5 (top panel) shows how varying  $N_{\text{fg}}$  influences  $\chi^2_{\text{dof}}$ , which should ideally be close to unity to represent a good model fit to the data with reasonably sized errors. For each  $N_{\text{fg}}$  case we recalculate the transfer function and re-fit the free parameter  $\Omega_{\text{H I}} b_{\text{H I}} r$  (values shown by the bottom panel), which avoids the  $\chi^2_{\text{dof}}$  improving simply because the amplitude of the power is decreasing into agreement with a pre-selected fiducial  $\Omega_{\text{H I}} b_{\text{H I}} r$ . We also show the cross-correlation detection strength, given by  $\sqrt{\Delta\chi^2}$ , on the right-hand (red) axis of Figure 5 (top panel).

At low  $N_{\text{fg}}$ , the  $\chi^2_{\text{dof}}$  appears reasonable but this is due to the larger statistical errors on the cross-power spectrum, which is fairly consistent with zero for these  $N_{\text{fg}}$ , as identified by the low detection significance in the  $\sqrt{\Delta\chi^2}$  results. The errors are larger for low  $N_{\text{fg}}$  because the residual foregrounds contribute significantly more variance to the maps, even though the residuals themselves are expected to correlate out on average. Increasing  $N_{\text{fg}}$  from 10 to 20 does little to improve the detection significance and initially worsens the  $\chi^2_{\text{dof}}$  caused by a decrease in error-bar size. At  $N_{\text{fg}} \sim 30$  enough components have been removed that a clear detection starts to manifest along with an improved agreement between data and model, given by the  $\chi^2_{\text{dof}} \sim 1$ . Going to much higher  $N_{\text{fg}}$  starts to over-clean the maps, reducing  $S/N$  and worsening the detection. To justify this explanation for the deterioration in results for  $N_{\text{fg}} > 30$ , we analysed the cross-correlation for maps constructed using just the principal components between 30 and 40. This map provided a  $\sim 3.4\sigma$  detection, indicat-

<sup>8</sup> MeerKAT dishes are 13.5 m in diameter and for comparison, the full-width-half-maximum for the central lobe from the beam is  $\sim 5$  times larger than the GBT (100 m dish diameter) observations at  $z \sim 0.8$ .

<sup>9</sup>  $\chi^2_{\text{dof}} \equiv \chi^2/\text{dof}$  where  $\text{dof}=24$  are the degrees of freedom which is the number of  $k$ -bins minus 1 for the single parameter we fit.

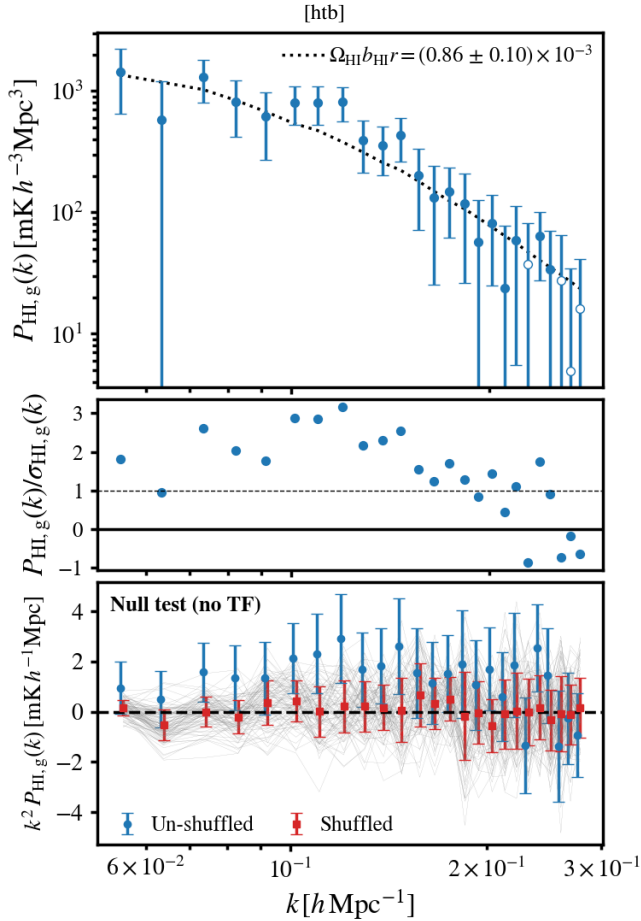


**Figure 4.** Cross power spectrum between WiggleZ galaxies and MeerKAT HI intensity maps cleaned by removing  $N_{\text{fg}} = 30$  PCA modes at  $0.400 < z < 0.459$ , with  $1\sigma$  error-bars (top panel). Hollow markers indicate a negative correlation. The black-dotted line represents a theoretical model (see Equation 17), fitted with an amplitude parameter  $\Omega_{\text{HI}} b_{\text{HI}} r$  given in the top-right. Calculating the  $\Delta\chi^2$  relative to a null-model ( $P_{\text{HI},g} = 0$ ) evaluates this as a  $7.7\sigma$  cross-correlation detection. The middle panel shows the ratio between data and error. The bottom panel shows a null test where the WiggleZ galaxy maps have had been shuffled along redshift. The thin grey lines show 100 different shuffles. The average (red squares) and standard deviation (red error bars) across the shuffled samples are shown relative to the original (blue-dots). In both cases in the bottom panel, no scaling by the transfer function has been applied.

ing that a lot of signal is present in the modes with  $30 < N_{\text{fg}} < 40$ , which explains the deterioration in  $\chi^2_{\text{dof}}$  beyond  $N_{\text{fg}} = 30$ , where these modes are gradually removed.

Figure 5 highlights the sensitivity of results to the foreground clean, and is further evidence that residual foregrounds and systematics are spread throughout the principal components. The ratio between systematics and signal varies among the various components thus some will be more influential on the cross-correlation than others. This causes a variation in the derived parameter  $\Omega_{\text{HI}} b_{\text{HI}} r$ , shown by the bottom panel of Figure 5. We estimate a contribution to the error budget of  $\Omega_{\text{HI}} b_{\text{HI}} r$  caused by the variance across the different  $N_{\text{fg}}$ , discussed further in the following section.

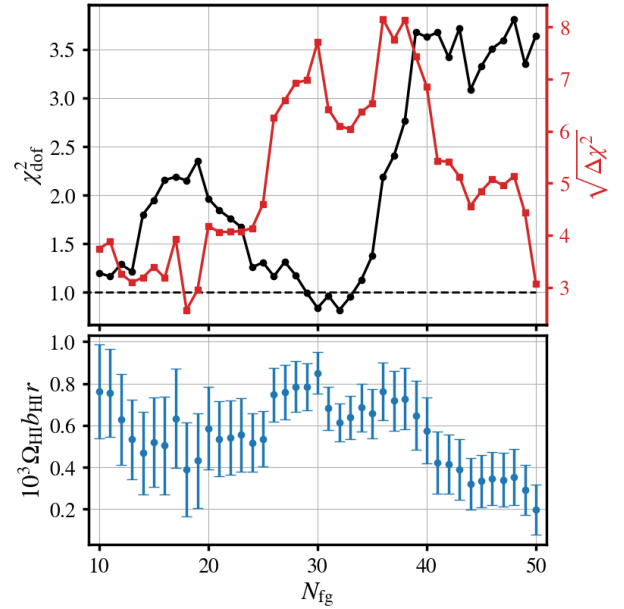


**Figure 5.** Sensitivity of results to foreground cleaning. Top panel, left-axis and black-dot data show the reduced  $\chi^2$  for each foreground cleaned cross-power spectra relative to its best-fit model. Top panel, right-axis and red-square data show the detection significance for the cross-power spectra relative to a null model. Bottom panel shows the variation in the best-fit  $\Omega_{\text{HI}} b_{\text{HI}} r$  for each  $N_{\text{fg}}$  case, from a least-squares fit to the cross-power spectrum amplitude.

#### 5.4 Constraints on $\Omega_{\text{HI}}$

Fitting the amplitude of the HI-galaxy cross-power spectrum provides a constraint on  $\Omega_{\text{HI}} b_{\text{HI}} r$  as a function of redshift. From our results in Figure 4, we find  $\Omega_{\text{HI}} b_{\text{HI}} r = [0.86 \pm 0.10 \text{ (stat)} \pm 0.12 \text{ (sys)}] \times 10^{-3}$ . The systematic error accounts for uncertainty from the map calibration and variance in results from the choice of  $N_{\text{fg}}$ . Firstly, uncertainty from the map calibration could cause a bias to the overall amplitude of the power spectrum. We address this by studying the residuals relative to the model in our calibration study (Wang et al. 2021). We are able to estimate that gain uncertainties should be at a level of  $\sim 2\%$ . Secondly, we account for the variance in results from the different number of PCA modes removed, indicative of residual systematics. We do this by evaluating the standard deviation on all  $\Omega_{\text{HI}} b_{\text{HI}} r$  fits (see Figure 5, bottom panel) from each reasonable choice of  $N_{\text{fg}}$  ( $10 < N_{\text{fg}} < 40$ ), which we find to be  $\sim 0.115$ , equating to a  $\sim 13\%$  error on  $\Omega_{\text{HI}} b_{\text{HI}} r$ . The combination of these two error components added in quadrature yields the systematic error in our final constraint.

The HI bias is not yet well understood but is expected to have some scale dependence when entering non-linear scales (high- $k$ ) (Villaescusa-Navarro et al. 2018; Spinelli et al. 2020). Furthermore, the cross-correlation coefficient  $r$ , included to account for stochasticity between the two fields, will also have some scale dependence. We therefore examined how the constraint on  $\Omega_{\text{HI}} b_{\text{HI}} r$  changed as we varied the scales at which it was measured. By cutting small- $k$  data points, we change the effective scale of the measurement, calculated by  $k_{\text{eff}} = \sum_i k_i (S/N)_i^2 / \sum_i (S/N)_i^2$ , where  $(S/N)_i$  is the signal-to-noise ratio in each  $k_i$  bin, i.e.  $\hat{P}_{\text{HI},g}(k_i) / \hat{\sigma}_{\text{HI},g}(k_i)$ . The scale dependence on the measurements of  $\Omega_{\text{HI}} b_{\text{HI}} r$  is shown in Figure 6 (red-star points) for  $N_{\text{fg}} = 30$ . The other coloured data points show previous intensity mapping constraints from GBT cross-correlation with galaxy surveys at  $z \sim 0.8$  (Wolz et al. 2022). The GBT inten-



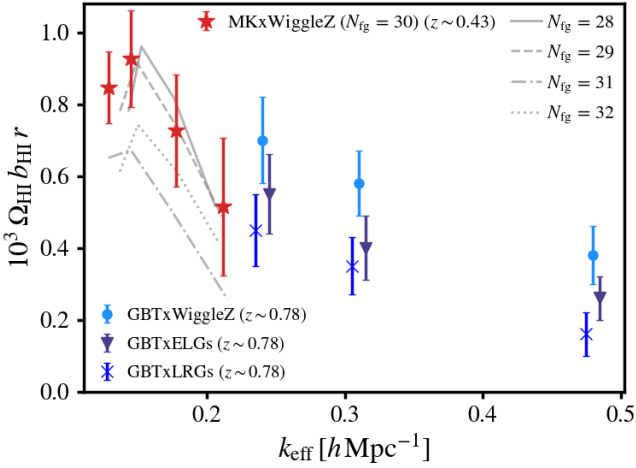


**Figure 6.** Constraints on  $\Omega_{\text{HI}} b_{\text{HI}} r$  measured at different effective scales  $k_{\text{eff}}$ , achieved by cutting low- $k$  data points from the cross-power spectrum, the data-points for each case are therefore not independent. The results for this paper are shown in red-stars using an  $N_{\text{fg}} = 30$  PCA clean and the four grey lines show results from different values of  $N_{\text{fg}}$ . For comparison we also plot the recent results from GBT cross-correlations (Wolz et al. 2022).

sity maps had a significantly smaller beam than MeerKAT thus were able to probe higher- $k$ . The MeerKAT and GBT measurements are at different redshifts so a direct comparison is not possible. Despite this, there still appears to be a trend with  $k_{\text{eff}}$  suggesting a detection of scale dependence in  $b_{\text{HI}} r$ . However, the continuity of the trend is affected by the choice of  $N_{\text{fg}}$ , as shown by the different grey lines in Figure 6. Furthermore, there is a possibility the scale dependence is influenced by systematics, which are mitigated in the scale cuts. The smallest- $k$  modes are the most affected by the transfer function, with up to 80% increase in amplitude (see Figure 3). Thus, further investigation is needed to disentangle the scale-dependence of  $b_{\text{HI}} r$  from possible scale-dependent systematics.

By making some further assumptions on  $b_{\text{HI}}$  and  $r$ , we can isolate the constraint on  $\Omega_{\text{HI}}$ . We assume  $r = 0.9 \pm 0.1$  (Khandai et al. 2011) and for the bias we interpolate between the hydrodynamic simulations in Villaescusa-Navarro et al. (2018) and use  $b_{\text{HI}} = 1.13 \pm 0.10$ . Fitting the power spectrum data in Figure 4 across all scales ( $k_{\text{eff}} \sim 0.13 \text{ h Mpc}^{-1}$ ), provides a constraint of  $\Omega_{\text{HI}} = [0.83 \pm 0.15 \text{ (stat)} \pm 0.11 \text{ (sys)}] \times 10^{-3}$  at the redshift of  $z = 0.43$ , which is reasonably consistent with other results in the literature (see comparison in Wolz et al. (2022)).

## 6 CONCLUSION

HI intensity mapping is a novel method for probing large scale cosmic structure and will be a primary objective for the future SKAO. To achieve this, it is necessary for the multi-dish array to operate in single-dish (auto-correlation) mode, as opposed to a conventional interferometer. In this work we have demonstrated, for the first time, the successful detection of cosmological signal using the MeerKAT multi-dish array in single-dish mode. This represents a major milestone in demonstrating the feasibility of this survey mode for SKAO.

We achieved this by cross-correlating 10.5 hrs of MeerKAT pilot survey intensity maps with overlapping optical galaxies from the WiggleZ Dark Energy Survey. A measurement of the cross-power spectrum between these fields provided a  $7.7\sigma$  detection

of a cross-correlation. We relied on an aggressive filtering process, removing 30 modes in a PCA-based foreground clean, necessary due to the presence of systematic contributions in the pilot survey data. This allowed us to obtain a constraint of  $\Omega_{\text{HI}} b_{\text{HI}} r = [0.86 \pm 0.10 \text{ (stat)} \pm 0.12 \text{ (sys)}] \times 10^{-3}$  from fitting the amplitude of the cross-power spectrum at an effective scale of  $k_{\text{eff}} \sim 0.13 \text{ h Mpc}^{-1}$ . Varying the effective scale of the measurement changed the value for  $\Omega_{\text{HI}} b_{\text{HI}} r$ , something noted in previous studies (Wolz et al. 2022). We also found  $\Omega_{\text{HI}} b_{\text{HI}} r$  to have a dependence on the number of foreground modes removed, so we included this variance in the systematic error budget of the constraint. The  $\sim 17.8\%$  precision represents a competitive  $\Omega_{\text{HI}} b_{\text{HI}} r$  constraint relative to other intensity mapping experiments. Furthermore, with additional assumptions on  $b_{\text{HI}}$  and  $r$ , we provided insight into the cosmic HI density  $\Omega_{\text{HI}}$ , for which measurements at higher redshifts are vital for understanding the evolution of HI.

The MeerKAT telescope will continue to conduct HI intensity mapping observations in single-dish mode. With enhanced calibration techniques and more observing time, improved constraints will be possible with less aggressive foreground removal. With this we can attempt a detection of the HI in auto-correlation, which is yet to be achieved. Observations have now been conducted in MeerKAT’s UHF band ( $0.40 < z < 1.45$ ), opening the possibility of higher redshift probes and for cross-correlating UHF-band data with the L-band data used in this work, with the aim of mitigating systematics.

## ACKNOWLEDGEMENTS

The authors would like to thank Stefano Camera for useful comments and questions during the development of this project. We would also like to thank Sourabh Paul for his comments on the final manuscript.

SC is supported by a UK Research and Innovation Future Leaders Fellowship grant [MR/V026437/1] and also acknowledges funding from the UK Research and Innovation Future Leaders Fellowship grant [MR/S016066/1]. MGS, YL and JW acknowledge support from the South African Radio Astronomy Observatory and National Research Foundation (Grant No. 84156). IPC acknowledges support from the ‘Departments of Excellence 2018-2022’ Grant (L. 232/2016) awarded by the Italian Ministry of University and Research (MUR). AP is a UK Research and Innovation Future Leaders Fellow [grant MR/S016066/1]. LW is a UK Research and Innovation Future Leaders Fellow [grant MR/V026437/1]. PS is supported by the Science and Technology Facilities Council [grant number ST/P006760/1] through the DISCnet Centre for Doctoral Training. This result is part of a project that has received funding from the European Research Council (ERC) under the European Union’s Horizon 2020 research and innovation programme (Grant agreement No. 948764; PB). PB acknowledges support from STFC Grant ST/T000341/1. JF acknowledges support from the Fundação para a Ciência e a Tecnologia (FCT) through the Investigador FCT Contract No. 2020.02633.CEECIND/CP1631/CT0002 and the research grants UIDB/04434/2020 and UIDP/04434/2020.

We acknowledge the use of the Ilifu cloud computing facility, through the Inter-University Institute for Data Intensive Astronomy (IDIA). The MeerKAT telescope is operated by the South African Radio Astronomy Observatory, which is a facility of the National Research Foundation, an agency of the Department of Science and Innovation.

For the purpose of open access, the author has applied a Creative Commons Attribution (CC BY) licence to any Author Accepted Manuscript version arising.

**DATA AVAILABILITY**

The data underlying this article will be shared upon acceptance of the manuscript.

**REFERENCES**

- Alonso D., Bull P., Ferreira P. G., Santos M. G., 2015, *Mon. Not. Roy. Astron. Soc.*, 447, 400
- Anderson C. J., et al., 2018, *Mon. Not. Roy. Astron. Soc.*, 476, 3382
- Asad K. M. B., et al., 2021, *MNRAS*, 502, 2970
- Battye R. A., Davies R. D., Weller J., 2004, *Mon. Not. Roy. Astron. Soc.*, 355, 1339
- Battye R. A., Browne I. W. A., Dickinson C., Heron G., Maffei B., Pourtsidou A., 2013, *Mon. Not. Roy. Astron. Soc.*, 434, 1239
- Bharadwaj S., Nath B., Nath B. B., Sethi S. K., 2001, *J. Astrophys. Astron.*, 22, 21
- Blake C., 2019, *Mon. Not. Roy. Astron. Soc.*, 489, 153
- Blake C., et al., 2010, *Mon. Not. Roy. Astron. Soc.*, 406, 803
- Blake C., et al., 2011, *Mon. Not. Roy. Astron. Soc.*, 415, 2876
- Bull P., Ferreira P. G., Patel P., Santos M. G., 2015, *Astrophys. J.*, 803, 21
- CHIME Collaboration et al., 2022, arXiv:2202.01242
- Chang T.-C., Pen U.-L., Peterson J. B., McDonald P., 2008, *Phys. Rev. Lett.*, 100, 091303
- Coles P., Jones B., 1991, *Mon. Not. Roy. Astron. Soc.*, 248, 1
- Cunnington S., 2022, *Mon. Not. Roy. Astron. Soc.*, 512, 2408–2425
- Cunnington S., Pourtsidou A., Soares P. S., Blake C., Bacon D., 2020, *Mon. Not. Roy. Astron. Soc.*, 496, 415
- Cunnington S., Irfan M. O., Carucci I. P., Pourtsidou A., Bobin J., 2021, *Mon. Not. Roy. Astron. Soc.*, 504, 208
- Drinkwater M. J., et al., 2010, *Mon. Not. Roy. Astron. Soc.*, 401, 1429
- Drinkwater M. J., et al., 2018, *Mon. Not. Roy. Astron. Soc.*, 474, 4151
- Feldman H. A., Kaiser N., Peacock J. A., 1994, *Astrophys. J.*, 426, 23
- Irfan M. O., et al., 2021, *Mon. Not. Roy. Astron. Soc.*, 509, 4923
- Jing Y. P., 2005, *Astrophys. J.*, 620, 559
- Kaiser N., 1987, *Mon. Not. Roy. Astron. Soc.*, 227, 1
- Khandai N., Sethi S. K., Di Matteo T., Croft R. A. C., Springel V., Jana A., Gardner J. P., 2011, *Mon. Not. Roy. Astron. Soc.*, 415, 2580
- Lewis A., Challinor A., Lasenby A., 2000, *Astrophys. J.*, 538, 473
- Li L., Staveley-Smith L., Rhee J., 2021a, *Res. Astron. Astrophys.*, 21, 030
- Li Y., Santos M. G., Grainge K., Harper S., Wang J., 2021b, *Mon. Not. Roy. Astron. Soc.*, 501, 4344
- Linder E. V., 2005, *Phys. Rev. D*, 72, 043529
- Masui K. W., et al., 2013, *Astrophys. J. Lett.*, 763, L20
- Matshawule S. D., Spinelli M., Santos M. G., Ngobese S., 2021, *Mon. Not. Roy. Astron. Soc.*, 506, 5075
- Norberg P., Baugh C. M., Gaztanaga E., Croton D. J., 2009, *Mon. Not. Roy. Astron. Soc.*, 396, 19
- Planck Collaboration et al., 2020, *Astron. Astrophys.*, 641, A1
- Pourtsidou A., Bacon D., Crittenden R., 2017, *Mon. Not. Roy. Astron. Soc.*, 470, 4251
- SKA Cosmology SWG 2020, *Publ. Astron. Soc. Austral.*, 37, e007
- Santos M. G., et al., 2017, in Proceedings, MeerKAT Science: On the Pathway to the SKA (MeerKAT2016): Stellenbosch, South Africa, May 25–27, 2016. ([arXiv:1709.06099](https://arxiv.org/abs/1709.06099))
- Soares P. S., Cunnington S., Pourtsidou A., Blake C., 2021, *Mon. Not. Roy. Astron. Soc.*, 502, 2549
- Spinelli M., Zoldan A., De Lucia G., Xie L., Viel M., 2020, *Mon. Not. Roy. Astron. Soc.*, 493, 5434
- Spinelli M., Carucci I. P., Cunnington S., Harper S. E., Irfan M. O., Fonseca J., Pourtsidou A., Wolz L., 2021, *Mon. Not. Roy. Astron. Soc.*, 509, 2048
- Switzer E. R., et al., 2013, *Mon. Not. Roy. Astron. Soc.*, 434, L46
- Switzer E. R., Chang T.-C., Masui K. W., Pen U.-L., Voytek T. C., 2015, *Astrophys. J.*, 815, 51
- Tegmark M., 1997, *Astrophys. J. Lett.*, 480, L87
- Tramonte D., Ma Y.-Z., 2020, *Mon. Not. Roy. Astron. Soc.*, 498, 5916
- Villaescusa-Navarro F., et al., 2018, *Astrophys. J.*, 866, 135
- Wang J., et al., 2021, *Mon. Not. Roy. Astron. Soc.*, 505, 3698
- Wolz L., Tonini C., Blake C., Wyithe J. S. B., 2016, *Mon. Not. Roy. Astron. Soc.*, 458, 3399
- Wolz L., et al., 2017, *Mon. Not. Roy. Astron. Soc.*, 464, 4938
- Wolz L., et al., 2022, *Mon. Not. Roy. Astron. Soc.*, 510, 3495
- Wyithe S., Loeb A., Geil P., 2008, *Mon. Not. Roy. Astron. Soc.*, 383, 1195
- de Villiers M. S., Cotton W. D., 2022, *Astron. J.*, 163, 135

This paper has been typeset from a  $\text{\TeX}/\text{\LaTeX}$  file prepared by the author.